Continuum Mech. Thermodyn. (2015) 27:433–446
DOI 10.1007/s00161-014-0371-8

ORIGINAL ARTICLE

Anirudh S. Rana · Alireza Mohammadzadeh · Henning Struchtrup

A numerical study of the heat transfer through a rarefied gas confined in a microcavity

Received: 25 October 2013 / Accepted: 1 July 2014 / Published online: 18 July 2014

Abstract Flow and heat transfer in a bottom-heated square cavity in a moderately rarefied gas is investigated using the R13 equations and the Navier–Stokes–Fourier equations. The results obtained are compared with those from the direct simulation Monte Carlo (DSMC) method with emphasis on understanding thermal flow characteristics from the slip flow to the early transition regime. The R13 theory gives satisfying results—including flow patterns in fair agreement with DSMC—in the transition regime, which the conventional Navier–Stokes–Fourier equations are not able to capture.

Keywords Rarefied gases · R13 equations · Navier–Stokes–Fourier equations · Slip–jump boundary conditions · Thermal cavity · Numerical heat transfer

1 Introduction

The design and performance optimization of microdevices such as micropumps, microactuators, microresonators, microsensors, and microheatexchangers [1–3] demands a good understanding of the heat transport mechanism through gases in rarefied conditions, where the physical length scales of devices are comparable with the mean free path of the gas. The degree of rarefaction in a gas is expressed by means of the Knudsen number Kn, which is defined as the ratio of the molecular mean free path λ to the macroscopic length scale of the flow, L, e.g., the diameter of a duct.

Based on the value of the Knudsen number, four flow regimes are distinguished in rarefied gas dynamics: [1,4] free molecular ($Kn \gtrapprox 10$), transition ($10 \gtrapprox Kn \gtrapprox 10^{-1}$), slip and jump ($10^{-1} \gtrapprox Kn \gtrapprox 10^{-3}$), and continuum regime ($10^{-3} \gtrapprox Kn$).

In the slip regime, effects such as velocity slip and temperature jump manifest themselves at the walls [5]. For the relevant range of Knudsen numbers, the Navier–Stokes equations can still be utilized with adapted boundary conditions allowing for velocity slip and temperature jump at the walls [6].

On the other hand, in the free molecular regime, the collisions of the gas molecules with surfaces prevail and the reflected molecules travel across a large distance before colliding with other molecules. Hence, the process is determined by the interaction between gas molecules and the surface, while collisions between the molecules in the gas may be neglected.

In the transition regime, however, due to insufficient collisions between gas molecules within the flow, the gas exhibits rarefaction effects such as Knudsen layers, Knudsen minimum, heat flux without temperature gradient, and thermal creep [6,7,9]. These effects cannot be described by the conventional continuum models

Communicated by Andreas Öchsner.

A. S. Rana (✉) · A. Mohammadzadeh · H. Struchtrup
Universiry of Victoria, Victoria, BC, Canada
E-mail: anirudh@uvic.ca

whose mathematical description is usually provided by the Navier–Stokes–Fourier (NSF) equations. Hence, the shear stresses and the heat fluxes can no longer be expressed as linear functions of the gradients in velocity and temperature.

The direct simulation Monte Carlo (DSMC) method is a commonly used method to investigate the flow and heat transfer behaviors in microdevices [4,10]. But this method is also very expensive both in computational time and memory requirements, especially for low-speed flow in microelectromechanical devices (MEMS) and nanodevices [11]. Recently, Hadjiconstaninou and co-workers developed a low-noise Monte Carlo method that greatly reduces the computational cost for linear problems [12].

The Boltzmann equation [5] gives an accurate microscopic description of gas flows at all Knudsen numbers, but its direct numerical solution requires huge computational effort [10]. A very common strategy in the literature is to consider simpler models for the collision term, typical examples are the BGK, ES-BGK, and S models [13]. These simplifications offer a significant computational advantage over the full collision operator in many practical situations [14,15]. In particular, for the slow flows, where DSMC method suffers from statistical noise, kinetic equations can be linearized and then they can be solved rather effectively by using the discrete velocity methods [16] or integro-moment methods [13].

An alternative is offered by macroscopic transport models, which capture microscale effects in a reasonable compromise between computational effort and required accuracy [17]. These approximation methods are obtained from the Boltzmann equation at different levels of accuracy. Conventionally, these high-order continuum models are derived based on either the Chapman–Enskog expansion method [18], or Grad's moment expansion method [19].

The Chapman–Enskog method relies on an asymptotic expansion of the Boltzmann equation in the Knudsen number. The NSF equations are obtained from first-order expansion, while the second-order and the third-order expansions give the Burnett and super-Burnett equations [17,20], respectively. However, these higher-order equations lack a complete set of boundary conditions and are usually unstable for time-dependent problems [21]. Recently, Bobylev suggested alternative forms of the Burnett equations that are, indeed, stable; however, at present, no boundary conditions are available for these equations [22,23].

In Grad's moment method, the set of macroscopic variables is extended beyond the hydrodynamic variables (mass density ρ, temperature T, velocity v_i) by including stress tensor σ_{ij}, heat flux vector q_i, and other higher moments of the distribution function. Grad's moments method offers no criterion on which moments need to be considered for a given Knudsen number.

The regularized-13 (R13) equations, see, e.g., Refs. [17,24–26], are obtained by combining the elements of the Chapman–Enskog and Grad methods, using the order of magnitude in the Knudsen number up to third order (super-Burnett order). The R13 equations are stable and equipped with a complete set of boundary conditions [27]. These equations provide an accurate description of rarefied gas flows for moderate Knudsen numbers, see Refs. [7,9,28,29], but at reasonable computational costs.

In the present work, the flow behavior and heat transfer characteristics of a rarefied gas confined in a bottom-heated square cavity [30–32] are investigated by solving the R13 equations and NSF equations numerically and comparing the results to DSMC solutions. Preliminary results for this problem were presented in Ref. [32]. Now, we consider a wider range of the temperature ratio to investigate also the nonlinear rarefaction effects, and we compare to DSMC simulations. An important point in this paper is that DSMC and R13 inform each other: We shall validate the R13 results by comparing to DSMC simulations and then, in turn, interpret the DSMC results in terms of macroscopic quantities.

The results show that for Knudsen numbers below 0.3, the main heat transfer characteristics are described reasonably well by the R13 equations, and slip and jump NSF equations, with higher accuracy offered by R13. The R13 equations can capture the main rarefaction effects, such as secondary eddies, in good accuracy, while the NSF equations fail to do so. The computational times are several orders of magnitude below the times required for the highly accurate DSMC simulations.

The rest of the paper is organized as follows: The physical model for the problem considered in this paper is described in Sect. 2. In Sect. 3.1, we present the R13 equations and the NSF equations for Maxwell molecules for steady-state process. Section 3.2 gives a short description on the theory of boundary conditions for the R13 equations, and the first-order slip and jump boundary conditions for the NSF equations. In Sect. 3.3, we summarize the numerical method and the DSMC method is presented in Sect. 3.4. In Sect. 4 of this article, we will discuss the effects of rarefaction on the flow and heat transfer characteristics. The paper ends with our conclusion given in Sect. 5.

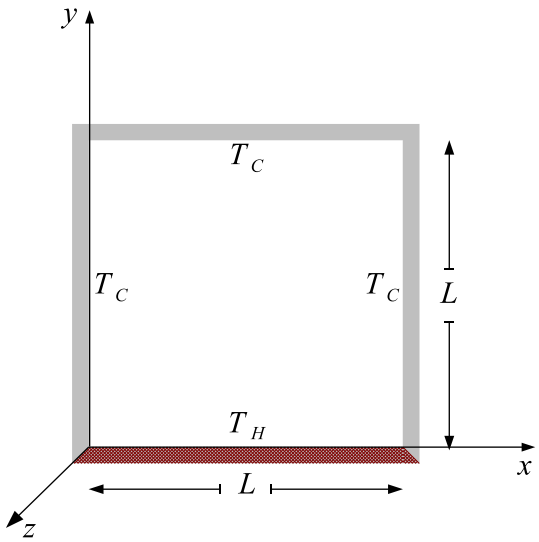

Fig. 1 Schematic of the problem with the imposed thermal conditions

2 Problem formulation

We consider the steady heat transfer through argon gas in a two-dimensional square cavity of side length L. The bottom surface of the cavity is kept at temperature T_H, and the other sides are maintained at temperature T_C, as shown in Fig. 1. The third dimension of the cavity is assumed to be large enough so that the fluid flow can be considered as two dimensional. Moreover, the effects of radiation and gravity are assumed to be negligible.

In the present study, the distance L between the plates is taken to be 1 μm and the average density, ρ_0, is varied to change the Knudsen number. The wall temperatures are fixed at $T_C = 300\,\mathrm{K}$ and $T_H = 600\,\mathrm{K}$. This large temperature difference is used since for smaller temperature differences, the DSMC method converges—in the Knudsen number range considered—very slowly. The reference viscosity of the argon gas at reference temperature $T_0 = 273\,\mathrm{K}$, according to [4], is $\mu_0 = 1.9552 \times 10^{-5}\ \mathrm{Ns/m^2}$. Temperature dependence of the viscosity $\hat{\mu}$ is given by

$$\hat{\mu} = \mu_0 \left(\frac{T}{T_0}\right)^{\omega} \tag{1}$$

with the temperature exponent $\omega = 1$, for Maxwell molecules.

3 Method of solution

With the Boltzmann equation as the starting point, the R13 equations [17,24] are obtained by combining the elements of the Chapman–Enskog and Grad methods. The goal of this macroscopic model is to reduce the high-dimensional phase space of the particle description to a low-dimensional continuum model by relating the physical quantities as moments of the probability density function.

The R13 equations, despite some limitation on the their accuracy at large Knudsen numbers ($Kn \gtrapprox 0.3$), elegantly explain all important rarefaction effects [6,7,28,29], which the classical hydrodynamic theory fails to describe.

Details of the derivation of the R13 equations can be found in [24] and the textbook Ref. [17], and the boundary conditions are presented in Ref. [27]. Here, we only present the final equations.

3.1 R13 equations

For steady flow in a rarefied gas, the non-dimensional governing equations expressing the conservation of mass, momentum, and energy are, in Cartesian coordinates, as follows:

$$\frac{\partial \rho v_k}{\partial x_k} = 0, \tag{2a}$$

$$\frac{\partial \left(p + \sigma_{ik} + \rho v_i v_k\right)}{\partial x_k} = 0, \tag{2b}$$

$$\frac{\partial \left(\frac{5p+\rho v^2}{2} v_k + \sigma_{ik} v_i + q_k\right)}{\partial x_k} = 0. \tag{2c}$$

Here, ρ, v_k, σ_{ik}, and q_k are the dimensionless mass density, velocity vector, stress tensor, and the heat flux vector, respectively. The pressure is given by the ideal gas law, $p = \rho\theta$, where temperature $\theta = RT$ and R is the specific gas constant. The dimensionless macroscopic properties of the gas are normalized by introducing

$$x_i = \frac{\widehat{x_i}}{L},\ \mu = \frac{\widehat{\mu}}{\mu_0}, \theta = \frac{T}{T_0}, \rho = \frac{\widehat{\rho}}{\rho_0}, v_i = \frac{\widehat{v_i}}{\sqrt{RT_0}}, q_i = \frac{\widehat{q_i}}{\rho_0 \sqrt{RT_0}^3}, \text{ and } \sigma_{ij} = \frac{\widehat{\sigma}_{ij}}{\rho_0 R T_0}.$$

The hat $\widehat{\ }$ over a quantity (e.g., $\widehat{\rho}$) represents the physical quantity with the proper dimensions. Moreover, ρ_0 is the average density, T_0 is the reference temperature, and μ_0 is the reference viscosity.

Closure of the conservation laws (2a–2c) requires specification of the stress tensor, σ_{ik}, and the heat flux vector, q_k, as constitutive equations. The Navier–Stokes–Fourier constitutive relations provide this additional closure information, these are Fourier's relation for heat conduction,

$$q_i = -Kn\mu \frac{15}{4} \frac{\partial \theta}{\partial x_i}, \tag{3}$$

and the Navier–Stokes relation for the viscous stress tensor of the Newtonian fluid,

$$\sigma_{ij} = -2Kn\mu \frac{\partial v_{\langle i}}{\partial x_{j\rangle}}\,. \tag{4}$$

The indices inside angular brackets denote the symmetric trace-free part of tensors [17]. As a result of non-dimensionalization, the Knudsen number, appearing in the governing equations, is defined as

$$Kn = \frac{\mu_0}{\rho_0 \sqrt{\theta_0}} \frac{1}{L}. \tag{5}$$

In the R13 system, the NSF laws are replaced by full balance equations for heat flux vector and stress tensor, which read

$$\frac{\partial \sigma_{ij} v_k}{\partial x_k} + \frac{4}{5} \frac{\partial q_{\langle i}}{\partial x_{j\rangle}} + 2\sigma_{k\langle i} \frac{\partial v_{j\rangle}}{\partial x_k} + \frac{\partial m_{ijk}}{\partial x_k} + \underline{2p \frac{\partial v_{\langle i}}{\partial x_{j\rangle}}} = \underline{-\frac{1}{Kn} \frac{p}{\mu} \sigma_{ij}}, \tag{6}$$

and

$$\begin{aligned} &\frac{\partial q_i v_k}{\partial x_k} + p \frac{\partial \left(\sigma_{ik}/\rho\right)}{\partial x_k} - \frac{\sigma_{ik}}{\rho} \frac{\partial \sigma_{kl}}{\partial x_l} + \frac{5}{2} \sigma_{ik} \frac{\partial \theta}{\partial x_k} + \frac{2}{5} q_i \frac{\partial v_k}{\partial x_k} + \frac{2}{5} q_k \frac{\partial v_k}{\partial x_i} \\ &\quad + \frac{7}{5} q_k \frac{\partial v_i}{\partial x_k} + \frac{1}{2} \frac{\partial R_{ik}}{\partial x_k} + \frac{1}{6} \frac{\partial \Delta}{\partial x_i} + m_{ikl} \frac{\partial v_k}{\partial x_l} + \underline{\frac{5}{2} p \frac{\partial \theta}{\partial x_i}} = \underline{-\frac{2}{3} \frac{1}{Kn} \frac{p}{\mu} q_i}\,. \end{aligned} \tag{7}$$

For $\Delta = R_{ij} = m_{ijk} = 0$, the above equations reduce to the well-known Grad's 13-moment equations [19]. The R13 closure for Δ, R_{ij}, and m_{ijk} results from higher-order moment equations, from which only terms are kept that influence heat flux and stress up to third order in the Knudsen number [7,28]. The original R13 equations, however, require a higher number of boundary conditions than the linearized equations [27]. To resolve this inconsistency, in Ref. [28], we used order of magnitude arguments to rewrite the nonlinear part of the R13 equations such that the third-order accuracy is maintained, but linear and nonlinear equations require the same number of boundary conditions. As a result, the constitutive relationships for Δ, R_{ij} and m_{ijk} read

$$\begin{aligned} \Delta &= 5\frac{\sigma_{kl}\sigma_{kl}}{\rho} + \frac{56}{5}\frac{q_k q_k}{p} - 12Kn\mu \left(\theta \frac{\partial \left(q_k/p\right)}{\partial x_k}\right), \\ R_{ij} &= \frac{20}{7}\frac{\sigma_{k\langle i}\sigma_{j\rangle k}}{\rho} + \frac{192}{75}\frac{q_{\langle i} q_{j\rangle}}{p} - \frac{24}{5} Kn\mu \left(\theta \frac{\partial \left(q_{\langle i}/p\right)}{\partial x_{j\rangle}}\right), \\ m_{ijk} &= \frac{20}{15}\frac{q_{\langle i}\sigma_{jk\rangle}}{p} - 2Kn\mu \left(\theta \frac{\partial \left(\sigma_{\langle ij}/p\right)}{\partial x_{k\rangle}}\right). \end{aligned} \tag{8}$$

A Chapman–Enskog expansion of Eqs. (6) and (7) shows that the NSF relations, as indicated by the underlined terms in (6) and (7), are included in the R13 equations asymptotically for small Knudsen numbers [17].

3.2 Boundary conditions for R13

The boundary conditions for the R13 equations are based on Maxwell's accommodation model, which assumes that a fraction $(1-\chi)$ of the gas molecules hitting the surface undergoes specular reflections, while the remaining fraction χ is diffusely reflected with a Maxwellian distribution f^W with the wall temperature θ^W and the tangential velocity v_τ^W of the wall. A detailed derivation of the R13 boundary conditions can be found in Ref. [27]; here, we just present the final result, a set of six boundary conditions for each wall,

$$v_n = 0 \tag{9a}$$

$$\sigma_{\tau n} = \frac{-\chi}{2-\chi}\sqrt{\frac{2}{\pi\theta}}\left(\mathcal{P}\mathcal{V}_\tau + \frac{1}{5}q_\tau + \frac{1}{2}m_{\tau nn}\right), \tag{9b}$$

$$q_n = \frac{-\chi}{2-\chi}\sqrt{\frac{2}{\pi\theta}}\left(2\mathcal{P}\mathcal{T} - \frac{1}{2}\mathcal{P}\mathcal{V}_\tau^2 + \frac{1}{2}\theta\sigma_{nn} + \frac{1}{15}\Delta + \frac{5}{28}R_{nn}\right), \tag{9c}$$

$$R_{\tau n} = \frac{\chi}{2-\chi}\sqrt{\frac{2}{\pi\theta}}\left(6\mathcal{P}\mathcal{T}\mathcal{V}_\tau + \mathcal{P}\theta\mathcal{V}_\tau - \mathcal{P}\mathcal{V}_\tau^3 - \frac{11}{5}\theta q_\tau - \frac{1}{2}\theta m_{\tau nn}\right), \tag{9d}$$

$$m_{nnn} = \frac{\chi}{2-\chi}\sqrt{\frac{2}{\pi\theta}}\left(\frac{2}{5}\mathcal{P}\mathcal{T} - \frac{3}{5}\mathcal{P}\mathcal{V}_\tau^2 - \frac{7}{5}\theta\sigma_{nn} + \frac{1}{75}\Delta - \frac{1}{14}R_{nn}\right), \tag{9e}$$

$$m_{\tau\tau n} = \frac{-\chi}{2-\chi}\sqrt{\frac{2}{\pi\theta}}\left(\frac{1}{5}\mathcal{P}\mathcal{T} - \frac{4}{5}\mathcal{P}\mathcal{V}_\tau^2 + \frac{1}{14}R_{\tau\tau} + \theta\sigma_{\tau\tau} - \frac{1}{5}\theta\sigma_{nn} + \frac{1}{150}\Delta\right), \tag{9f}$$

where

$$\mathcal{P} = \rho_W\sqrt{\theta_W}\sqrt{\theta} = \left(\rho\theta + \frac{1}{2}\sigma_{nn} - \frac{1}{120}\frac{\Delta}{\theta} - \frac{1}{28}\frac{R_{nn}}{\theta}\right). \tag{10}$$

Here, $\mathcal{V}_\tau = v_\tau - v_\tau^W$ and $\mathcal{T} = \theta - \theta^W$ are velocity slip and temperature jump, respectively. The subscript n denotes the direction of the wall normal pointing toward the gas, and τ is the tangential direction relative to the wall.

The first-order slip and jump boundary conditions for the NSF equations are obtained from Eqs. (9a)–(9c) by retaining the terms only up to first order and replacing the stress tensor, σ_{ik}, and the heat flux vector, q_k, from the Navier–Stokes–Fourier constitutive relations (4) and (3) [17]; they read

$$v_n = 0, \tag{11a}$$

$$\sigma_{\tau n} = \frac{-\chi}{2-\chi}\sqrt{\frac{2}{\pi\theta}}\left(\mathcal{P}\mathcal{V}_\tau + \frac{1}{5}q_\tau\right), \tag{11b}$$

$$q_n = \frac{-\chi}{2-\chi}\sqrt{\frac{2}{\pi\theta}}\left(2\mathcal{P}\mathcal{T} + \frac{1}{2}\theta\sigma_{nn}\right). \tag{11c}$$

Equations (9b) or (11b) relate the velocity slip $\mathcal{V}_\tau$ to the shear stress $\sigma_{\tau n}$, associated with the gradient of tangential velocity in the normal direction, and the heat flux q_τ, tangential to the boundary. The latter term can induce a flow from the colder to the hotter part of the gas, an effect usually referred to as thermal transpiration [6]. Similarly, the next Eq. (11c) gives the temperature jump $\mathcal{T}$ in terms of normal components of heat flux vector and stress tensor.

3.3 Numerical method

A second-order central finite-difference scheme was employed to obtain a numerical solution of the R13 and NSF equations in Ref. [28]. The discretized equations obtained were solved iteratively, with a quasi-minimal residual (QMR) algorithm using MATLAB. The nonlinear terms were substituted successively with

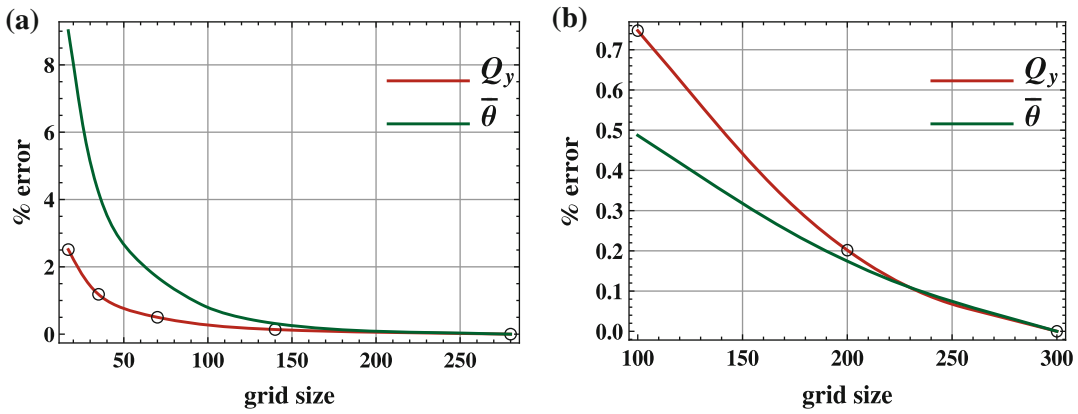

Fig. 2 Grid independence test of the numerical solution in terms of Q_y and $\bar{\theta}$ for $Kn = 0.13$. **a** R13 solution and **b** DSMC method

updated values. The solution was considered to be fully converged when the maximum absolute values of the dependent variables at any node from iteration to iteration are smaller than a prescribed value, chosen as 10^{-5}. The simulations were conducted using a two-dimensional grid with 120×120 uniformly spaced grid points. A grid independence test was conducted with different meshes of size $N = 17, 35, 70, 140, 280$. Figure 2a shows, for various mesh sizes, the relative change in the net dimensionless heat transfer from the bottom surface,

$$Q_y = \frac{1}{N} \sum_{i=1}^{N} (q_y)_{i,1} ,$$

and the average temperature along the heated surface,

$$\bar{\theta} = \frac{1}{N} \sum_{i=1}^{N} \theta_{i,1} .$$

The maximum deviations observed in terms of Q_y and $\bar{\theta}$ remain within 0.61 and 0.41 %, respectively, when the grid of 120×120 is considered. This justifies the selected grid size 120×120 as a reasonable compromise between computational effort and required accuracy. A typical simulation with R13 equations (as well as NSF), when a grid of size 120×120 is considered, takes about 20 min on a single quad-core desktop PC. Whereas depending on the flow parameters and the value of the Knudsen number, DSMC simulation takes up to 70 h of the computational time.

3.4 DSMC method

The DSMC method used in this paper follows the scheme proposed by Bird [4]. The DSMC method is a particle method based on the kinetic theory for the simulation of the dilute gases, where the dynamic equations for a gas are solved for simulated particles. Each particle represents a large number of real gas molecules and mimics the actual physics by interacting with other particles and solid surfaces. The local macroscopic quantities are obtained by averaging the molecular properties in each cell. The time step Δt in the DSMC method is chosen so small that the motion of particles and their collisions can be decoupled at each time step. In order to implement DSMC, the domain is first divided into computational cells. The cell size should be chosen small enough so that the changes in the thermodynamic flow properties are small across each cell. The cells are then divided into subcells in each direction to facilitate the selection of collision pairs. In the current study, Maxwell argon particles with $m = 6.63 \times 10^{-26}$ kg and reference viscosity of $\mu_0 = 1.9549 \times 10^{-5}$ Pa·s are considered. The particle diameter, d, is related to the reference viscosity as [4]

$$d^2 = \frac{5\,(\alpha+1)\,(\alpha+2)\,\sqrt{mkT_0/\pi}}{4\alpha\,(5-2\omega)\,(7-2\omega)\,\mu_0},$$

with $\alpha = 2.13986$ and $\omega = 1$ for Maxwell molecules [4], k is the Boltzmann constant. To satisfy the cell size limitation, the cell dimensions Δx, Δy are considered as 0.1λ; to reduce the scattering noises, 64 particles are initially set in each computational cell.

For gas–solid interaction, Maxwell's accommodation model is employed. The accommodation coefficient χ is assigned the value of unity, i.e., fully diffuse reflection has been assumed for all DSMC solutions. In order to minimize the statistical scattering, molecular properties are sampled over a large period of time after the flow reaches steady state. These time-averaged data are then used to obtain the thermodynamic parameters such as velocity, temperature, and heat flux. In addition, a filtering post-processor in DSMC is used to minimize the scattering in the predicted results. In this filtering, the sampled macroscopic properties, F, in cell N are averaged over a pattern of its neighboring cells,

$$\widetilde{F}_{(N)} = \frac{F_N + \sum_{I=1}^{I=N_n} F_I}{N_n + 1},$$

where N_n denotes the four neighboring cells located at the above, below, left, and right side of the cell N.

In order to perform the grid independency test, we considered four grids composed of 50×50, 100×100, 200×200, and 300×300 cells. Relative percentage changes in the net dimensionless heat transfer and the average temperature along the heated surface are plotted in Fig. 2b. It is seen that the results are numerically equivalent for 200×200 and 300×300 grids, with the relative errors less than 0.2 % for both Q_y as well as $\bar{\theta}$. Therefore, the grid containing 200×200 cells is selected for the reported results of the DSMC method in this study.

4 Results and discussion

4.1 Analysis of streamlines and isotherms

Figure 3 shows the velocity streamlines superimposed on the temperature contours resulting from the Navier–Stokes–Fourier, DSMC, and the R13 theory, respectively, at $Kn = 0.05$. The NSF results show two counter-circulating primary vortices, symmetrical with respect to the center of the cavity. The flow velocity is relatively small indicating a rather slow convective motion ($v \approx 0.1$ m/s). The formation of the primary vortices is due to the sharp temperature gradients in the corners between the heated and cooled walls, which induce thermal transpiration. As can be seen from the figures, the isotherms near the corners are visibly denser, which indicates higher temperature gradients in this region.

Interestingly, in addition to the primary vortices, the R13 equations and the DSMC both predict two secondary counter-circulating vortices located along the vertical cold surfaces. The formation of the secondary vortices can be explained by the different terms in the slip boundary condition (9b), which reads

$$-v_y \approx \frac{1}{\mathcal{P}}\left(\sqrt{\frac{\pi\theta}{2}}\sigma_{xy} + \frac{1}{5}q_y\right) = v_y^{vis} + v_y^{tra}. \tag{12}$$

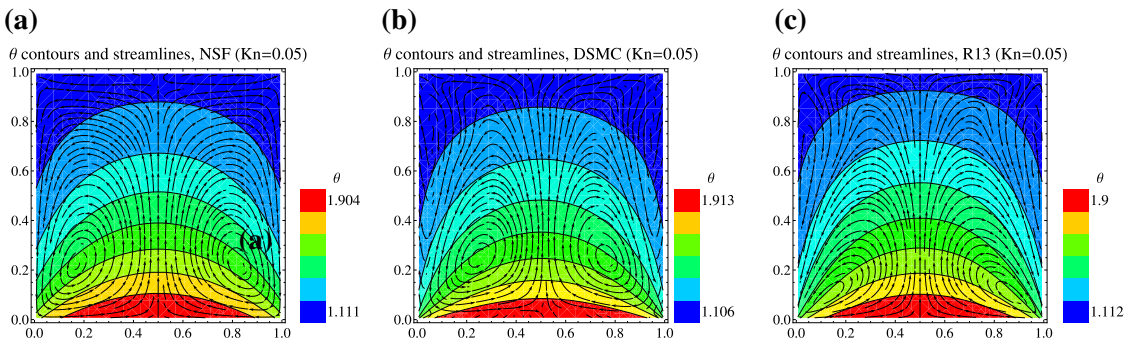

Fig. 3 Streamlines and temperature contours for $Kn = 0.05$. **a** NSF solutions, **b** DSMC solutions, and **c** R13 solutions

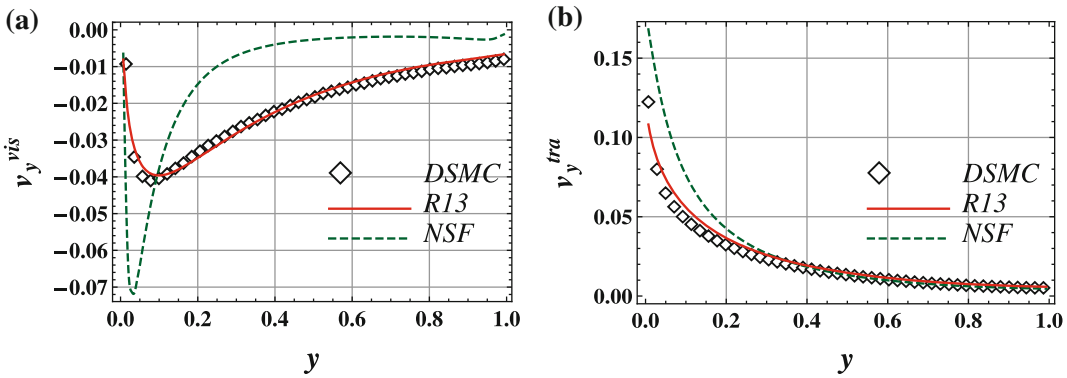

Fig. 4 Variations in the viscous velocity and the transpirational velocity for $Kn = 0.05$. **a** viscous and **b** transpirational contribution to the velocity slip

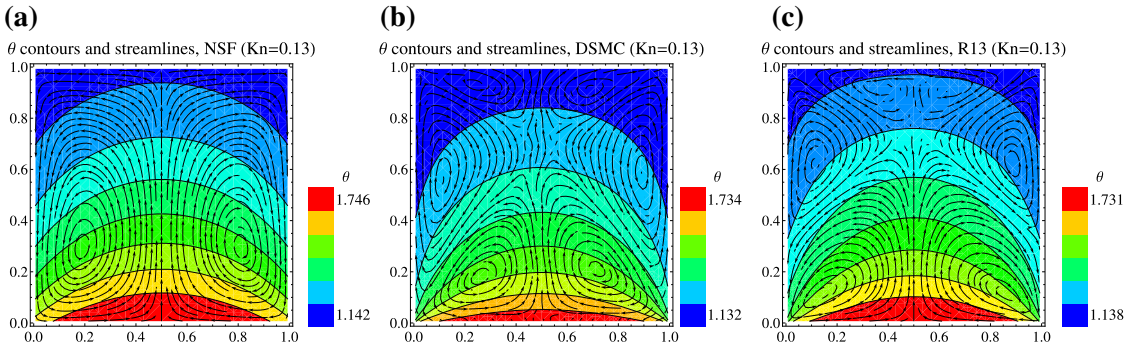

Fig. 5 Streamlines and temperature contours for $Kn = 0.13$. **a** NSF solutions, **b** DSMC solutions, and **c** R13 solutions

Variations in the viscous velocity, $v_y^{vis} = \frac{1}{\mathcal{P}}\sqrt{\frac{\pi\theta}{2}}\sigma_{xy}$, and the transpirational velocity, $v_y^{tra} = \frac{1}{\mathcal{P}}\frac{1}{5}q_y$, evaluated along $x = 0$, are presented in Fig. 4, for NSF, DSMC, and R13 solutions. Along the vertical surface, $x = 0$, the viscous velocity is negative, thus inducing a flow in the upward direction.

On the other hand, the transpirational velocity is positive (heat flows upwards, from hot to cold), inducing consequently a flow in downward direction, from the colder to the hotter region. Hence, both terms induce flows in opposite direction. The respective magnitude of these terms determines the actual local direction of the flow along $x = 0$.

For DSMC, the viscous contribution is larger than the transpiration term, hence the secondary vortices appear. NSF equations are unable to produce the secondary vortices, since for them the transpirational velocity along the vertical wall dominates the viscous velocity. The R13 equations, however, give a better description of stress and heat flux and capture the formation of secondary whirls.

By increasing the Knudsen number to 0.13 (Fig. 5), the fluid circulation becomes more intense. The flow structure for NSF remains bicellular, whereas R13 as well as DSMC predict the appearance of two additional small vortices located near the upper surface of the cavity. For the NSF equations, the isotherms exhibit smaller curvature near the vertical sidewalls. A further increase to $Kn = 0.3$ leads to significant changes in the flow fields, as can be observed in Fig. 6. For the DSMC simulation, the secondary vortices span most of the cavity area, whereas for R13 the secondary eddies extend only about the upper half of the domain.

From the differences to the DSMC results, it becomes obvious that this Knudsen number is outside of the range of applicability of both the R13 and the NSF theories. However, the qualitative description given by the R13 equations is comparable with DSMC, while NSF cannot describe the flow features.

4.2 Analysis of heat flux lines and shear stress distribution

Figure 7 shows heat flux lines superimposed on viscous shear stress contours (σ_{xy}) for $Kn = 0.05$, computed with NSF, DSMC, and R13, respectively. The distribution of heat flux lines is similar for the NSF, R13, and

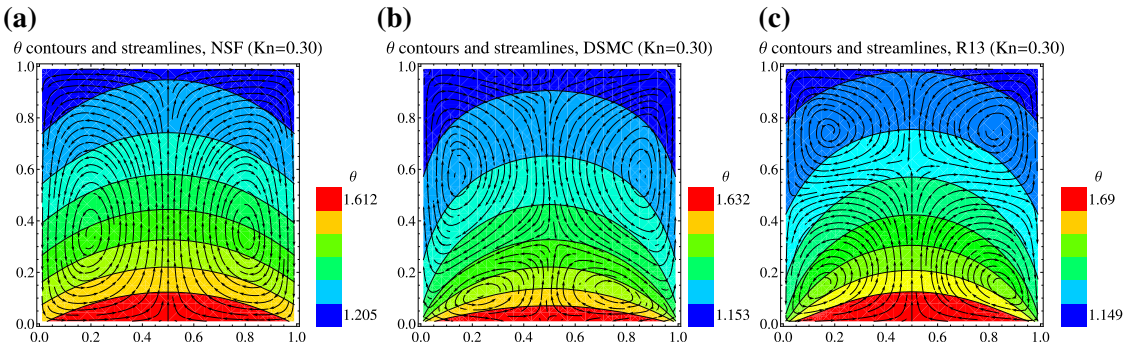

Fig. 6 Streamlines and temperature contours for $Kn = 0.30$. **a** NSF solutions, **b** DSMC solutions, and **c** R13 solutions

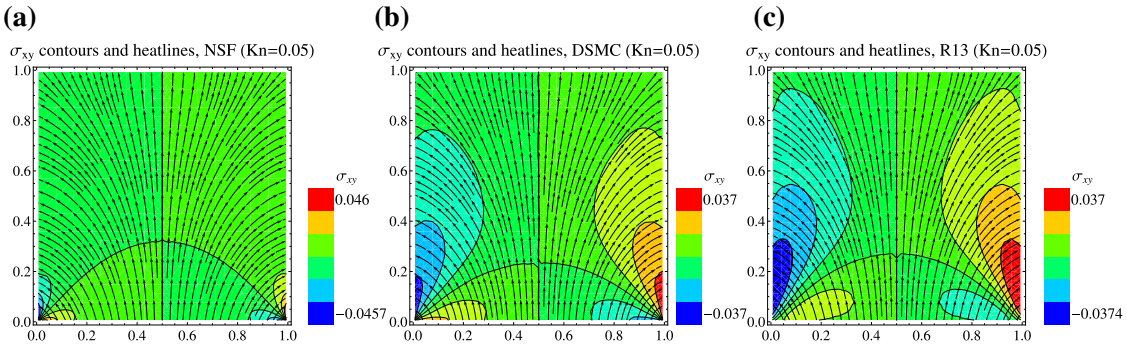

Fig. 7 Heat flux lines and shear stress contours for $Kn = 0.05$. **a** NSF solutions, **b** DSMC solutions, and **c** R13 solutions

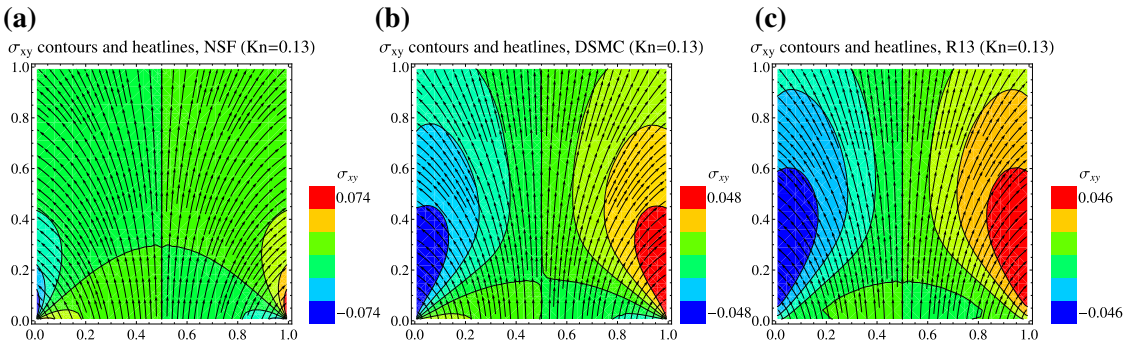

Fig. 8 Heat flux lines and shear stress contours for $Kn = 0.13$. **a** NSF solutions, **b** DSMC solutions, and **c** R13 solutions

the DSMC solutions, indicating a dominating Fourier heat transfer contribution, but, as will be seen in the next section, the actual values for heat transfer differ markedly.

As far as the shear stresses are concerned, DSMC (Fig. 7b) and R13 (Fig. 7c) show relatively similar shear stress contours, which differ from the NSF contours (Fig. 7a) already at $Kn = 0.05$. The DSMC and the R13 solutions show more uniform stress fields in the vicinity of the corners between the heated and cooled walls, whereas the NSF solutions show the stress localized to the lower corners.

With increase to $Kn = 0.13$, shown in Fig. 8, the corresponding heat flux lines exhibit relatively small divergence toward the vertical sidewalls indicating a weaker heat exchange between the bottom surface and the vertical surfaces.

4.3 Effect of Knudsen number on heat flux

Figure 9 illustrates the variation in the normal heat flux, q_y, along the bottom plate, obtained by solving R13 (solid curve), NSF (dashed curves), and DSMC (symbols). The results show that the normal heat flux

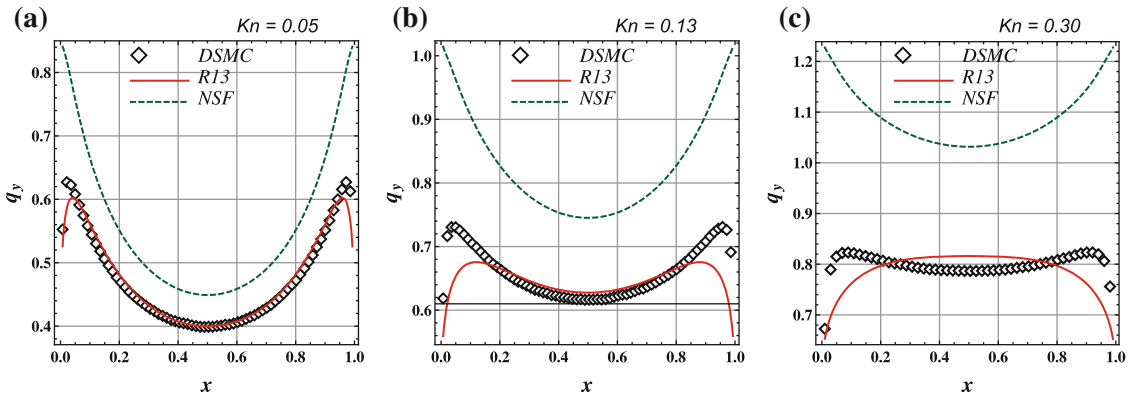

Fig. 9 Normal heat flux, q_y, along the bottom plate, obtained by solving R13 (*solid curve*), NSF (*dashed curves*) and DSMC (*symbols*). **a** $Kn = 0.05$, **b** $Kn = 0.13$ and **c** $Kn = 0.3$

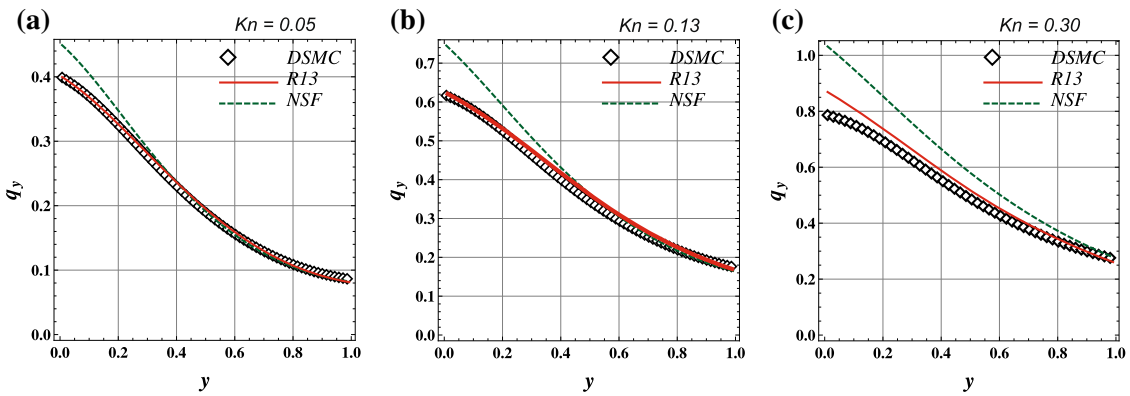

Fig. 10 Normal heat flux, q_y, along the centerline of the cavity, obtained by solving R13 (*solid curve*), NSF (*dashed green curves*) and DSMC (*symbols*). **a** $Kn = 0.05$, **b** $Kn = 0.13$, and **c** $Kn = 0.3$

calculated by the R13 equations agrees with the DSMC solution at smaller Knudsen numbers (Figs. 9 a, b). At larger Knudsen number, $Kn = 0.3$ in Fig. 9c, the R13 equations underpredict the normal heat flux by 5 %. The Navier–Stokes–Fourier's equations, however, predict approximately 15 % higher normal heat flux than DSMC, already at small Knudsen number of 0.05. By increasing the Knudsen number value to 0.13 and 0.3, the NSF equations overpredict the normal heat flux by as much as 25 and 35 %, respectively.

Higher Knudsen numbers show stronger non-equilibrium as indicated by larger magnitudes of q_y. Interestingly, the normal heat flux along the bottom plate, predicted by DSMC, shows a bimodal behavior. This can also be observed in the results of the R13 system in Fig. 9, while the NSF system fails to capture this.

The simulation results for the normal heat flux along the centerline of the cavity at $Kn = 0.05, 0.13, 0.3$ are shown in Fig. 10. As before, the simulation results of DSMC are compared with the NSF and the R13 predictions. The R13 theory follows the DSMC result fairly accurate until $Kn \lesssim 0.3$.

The average dimensionless heat transfer along the heated element, defined as

$$Q_y = \int_0^1 q_y\,(x, 0)\,dx, \tag{13}$$

is shown in Fig. 11 for Knudsen numbers below 0.4.

The figure shows a monotonous increase of Q_y with Kn for all three theories. It can be seen that the increase rate of heat transfer is larger for the NSF model than that corresponding to DSMC and R13.

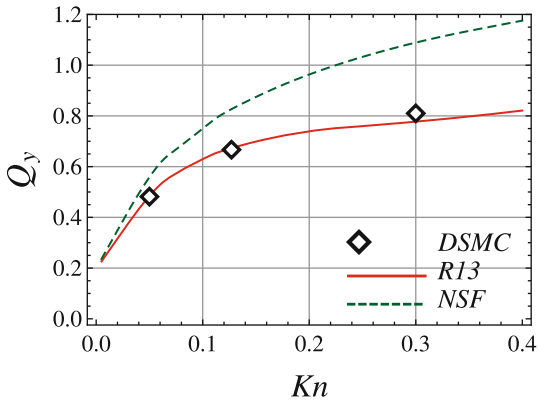

Fig. 11 Average dimensionless heat transfer along the heated element, Q_y, for various Kn

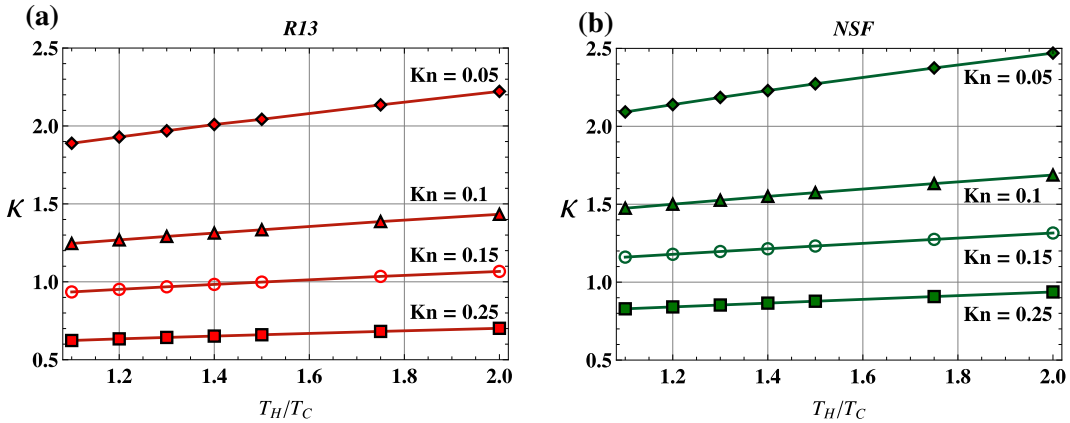

Fig. 12 Dimensionless effective heat conductivity, κ, in terms of T_H/T_C for various values of Kn. **a** R13, **b** NSF

4.4 Influence of temperature ratio

In Fig. 12, numerical results for the dimensionless effective heat conductivity, defined as

$$\kappa = \frac{Q_y}{\frac{15}{4} Kn\,(\theta_H - \theta_C)}, \tag{14}$$

are shown for temperature ratios $1.1 \leq T_H/T_C \leq 2$, for various values of the Knudsen numbers. Results on the dimensionless effective heat conductivity, based on the R13 and NSF theories, are presented in Fig. 12a, b, respectively, for $T_C = T_0 = 273$ K. It is seen from Fig. 12 that the conductivity is decreased as Kn is increased. This behavior is expected since increasing the Knudsen number diminishes the intermolecular collisions in the gas, and consequently, the effective heat conductivity is decreased. Furthermore, as the temperature ratio, T_H/T_C, is increased, the effective heat conductivity is also increased. For all cases, NSF predicts a larger effective heat conductivity than R13. This matches our earlier observation that NSF drastically overpredicts the heat transfer (see Fig. 9).

The combined effects of the temperature ratio, T_H/T_C, and the Knudsen number, Kn, on the flow structure will be examined next. Results are reported in terms of isotherms and streamlines. These observations are shown by the plots in Fig. 13 ($Kn = 0.05$) and 14 ($Kn = 0.1$).

Figure 13a, b, and c illustrate the results obtained from R13 equation for the temperature ratio T_H/T_C = 1.1, 1.5, and 2, respectively, for the Knudsen number 0.05. The streamlines indicate that the secondary vortices grow along the vertical cold surfaces as the temperature ratio is increased.

The flow field for $Kn = 0.1$, shown in Fig. 14, shows hardly visible secondary cells at low temperature ratio. These grow as the temperature ratio is increased, and an additional cell flow pattern develops as T_H/T_C reaches 2.

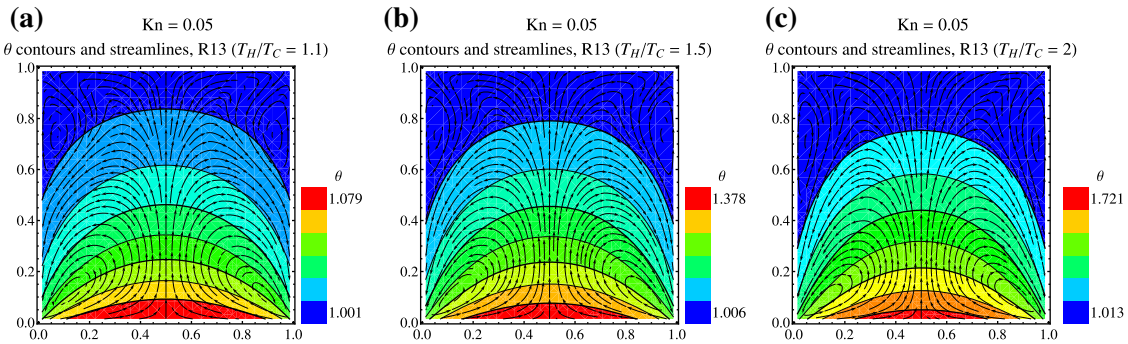

Fig. 13 Streamlines and temperature contours for $Kn = 0.05$ for R13 equations at various values of the temperature ratio, T_H/T_C. **a** $T_H/T_C = 1.1$, **b** $T_H/T_C = 1.5$, and **c** $T_H/T_C = 2$

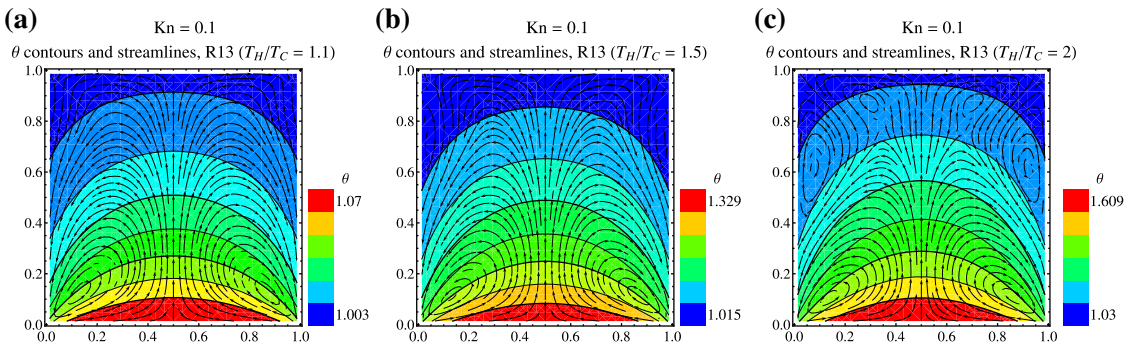

Fig. 14 Streamlines and temperature contours for $Kn = 0.1$ for R13 equations at various values of the temperature ratio, T_H/T_C. **a** $T_H/T_C = 1.1$, **b** $T_H/T_C = 1.5$, and **c** $T_H/T_C = 2$

4.5 Effects of convection on effective heat conductivity

In order to evaluate the influence of convection upon the effective heat conductivity, defined in Eq. (14), we compare results for the R13 equations and the NSF equations in the moving gas with those for a gas at rest. For this, we solve the NSF (and the R13) equations with zero velocity throughout, $v_i = 0$, for example, in the NSF case the Eqs. (2c) and (3) simplify to

$$\frac{\partial q_k}{\partial x_k} = 0, \quad \text{and} \quad q_i = -Kn\mu \frac{15}{4} \frac{\partial \theta}{\partial x_i}.$$

The corresponding boundary condition, from the Eq. (11c), reads

$$q_n = \frac{-2\chi}{2-\chi} \sqrt{\frac{2}{\pi\theta}} \rho\theta\mathcal{T}.$$

The results computed from the R13 equations (stationary and the moving gas) are shown in Fig. 15a, where the dashed curves are for the gas at rest and the continuous curves for the moving gas. The corresponding results computed with the NSF equations are presented in Fig. 15b. As we see from Fig. 15, for both continuum models, the effective heat conductivity in the pure heat conduction case ($v_i = 0$) is slightly higher than the effective heat conductivity in a moving gas; hence, the heat transfer is slightly weakened by convection. At small temperature, ratios NSF and R13 both show a very small difference (less than 2 %) between the heat conductivity in a moving and a stationary gas. At temperature ratio 2, this difference increases slightly up to 3–4 %. We note that a comparable test is not possible in the classical DSMC method, since there the macroscopic gas velocity v_i cannot be controlled.

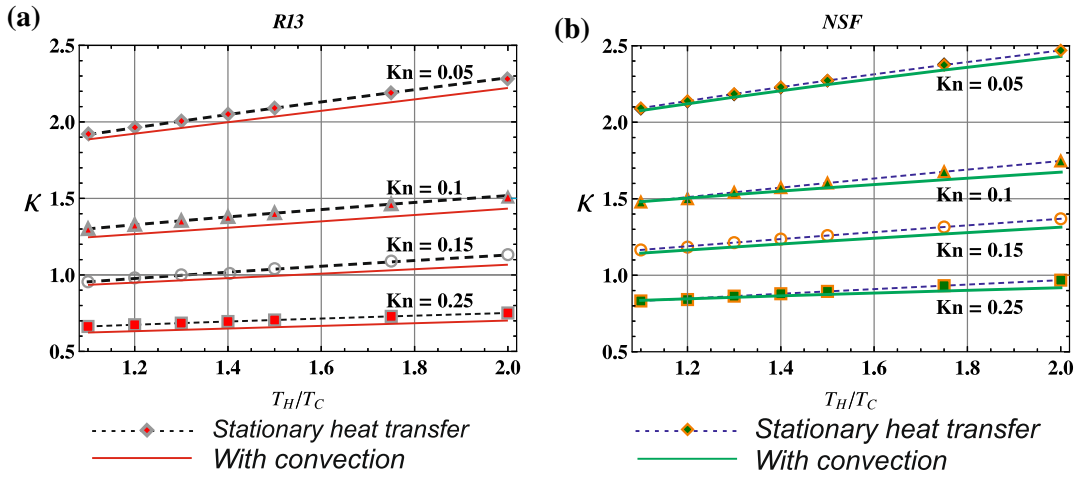

Fig. 15 Effective heat conductivity is compared between a stationary gas (*dashed curves*) against the effective heat conductivity (*continuous curves*) in a moving gas, in terms of T_H/T_C for various values of Kn. **a** R13, **b** NSF

5 Conclusions

Numerical simulations were performed for various Knudsen numbers to investigate the effects of rarefaction on the flow and heat transfer characteristics in a thermal cavity using Navier–Stokes–Fourier equations with first-order jump and slip boundary conditions and the R13 equations. The results obtained are compared with those from the DSMC method. We observed that the DSMC shows a bimodal behavior for the normal heat flux along the bottom plate. This behavior of the normal heat flux is correctly predicted by the R13 equations, while the NSF equations fail to capture this. Moreover, the DSMC results show significant flow patterns, which are absent in the NSF theory. This convective mechanism in the gas was described in detailed through relative terms in the boundary conditions and their respective size. Our results show that the R13 equations yield satisfactory agreement with DSMC data—including flow patterns—in the transition regime for Knudsen numbers below 0.3.

Combined effects of the temperature ratio, T_H/T_C, and the Knudsen number, Kn, on the effective heat conductivity and flow structure were examined. The results show that the heat flux increases monotonically with temperature ratio, and the heat flux is decreased as Kn increased. Here, we have considered the R13 equations for Maxwell molecules, for which the derivation of moment equations is comparatively easy, and which are now well established for the linear and nonlinear cases. Only recently, the R13 equations were extended for the hard-sphere model [26], where presently only the linear equations are available. Already at the hydrodynamic level, different molecular interaction potentials for the collision term yield different transport parameters, e.g., the temperature exponent in viscosity ω for hard spheres is 0.5, for Maxwell molecules it is 1, whereas the measured value of ω is 0.81.

It is straightforward to incorporate the different temperature dependence of viscosity and a different Prandtl number into the moment equations. However, for higher moment theories such as R13 or Burnett equations, not only the viscosity and heat conductivity vary with collision model but also other transport parameters change with the molecular interaction potentials [26]. For instance, almost all coefficients in the R13 equations change their values when the equations are derived for hard spheres [26]. Therefore, it is expected that differences in transport parameters due to different molecular interaction potentials will lead into small differences in transport quantities. The effects of the different interaction potential are planned for the future; this requires the derivation of R13 boundary conditions for the hard-sphere case, which are presently not available.

We reiterate that the R13 equations can be solved in rather short computational time as compared to those for the DSMC method, while, in the appropriate range of Knudsen numbers, they give results in remarkable agreement to DSMC.

Acknowledgments This research was supported by the Natural Sciences and Engineering Research Council (NSERC).

References

1. Gad-el-Hak, M.: The MEMS Handbook, vol. I–III, 2nd edn. CRC Press, Boca Raton (2005)
2. Ho, C.M., Tai, Y.C.: Micro-electro-mechanical-systems (MEMS) and fluid flows. Ann. Rev. Fluid Mech. **30**, 579 (1998)
3. Karniadakis, G.E., Beskok, A.: Micro Flows: Fundamentals and Simulation. Springer, New York (2002)
4. Bird, G.A.: Molecular Gas Dynamics and the Direct Simulation of Gas Flows. Oxford University Press, Oxford (1994)
5. Cercignani, C.: Theory and application of the Boltzmann equation. Scottish Academic Press, Edinburgh (1975)
6. Sone, Y.: Kinetic Theory and Fluid Dynamics. Birkh äuser, Boston (2002)
7. Struchtrup, H., Taheri, P.: Macroscopic transport models for rarefied gas flows: a brief review. IMA J. Appl. Math. **76**(5), 672 (2011)
8. Mizzi, S., Barber, R.W., Emerson, D.R., Reese, J.M., Stefanov, S.K.: A phenomenological and extended continuum approach for modelling non-equilibrium flows. Contin. Mech. Thermodyn. **19**, 273 (2007)
9. Taheri, P., Rana, A.S., Torrilhon, M., Struchtrup, H.: Macroscopic description of steady and unsteady rarefaction effects in boundary value problems of gas dynamics. Contin. Mech. Thermodyn. **21**, 423 (2009)
10. Hadjiconstantinou, N., Garcia, A., Bazant, M., He, G.: Statistical error in particle simulations of hydrodynamic phenomena. J. Comput. Phys. **187**, 274–297 (2003)
11. Fan, J., Shen, C.: Statistical simulation of low-speed rarefied gas flows. J. Comput. Phys. **167**, 393 (2001)
12. Radtke, G.A., Hadjiconstantinou, N.G.: Variance-reduced particle simulation of the Boltzmann transport equation in the relaxation-time approximation. Phys. Rev. E **79**, 056711 (2009)
13. Sharipov, F., Seleznev, V.: Data on internal rarefied gas flows. J. Phys. Chem. Ref. Data **27**(3), 657–706 (1998)
14. Varoutis, S., Valougeorgis, D., Sharipov, F.: Application of the integro-moment method to steady-state multidimensional rarefied gas flows subject to boundary induced discontinuities. J. Comput. Phys. **227**, 6272–6287 (2008)
15. Naris, S., Valougeorgis, D., Kalempa, D., Sharipov, F.: Flow of gaseous mixtures through rectangular microchannels driven by pressure, temperature and concentration gradients. Phys. Fluids **17**(10), 100607 (2005)
16. Aristov, V.V.: Direct Methods for Solving the Boltzmann Equation and Study of Nonequilibrium Flows. Kluwer Academic Publishers, Dordrecht (2001)
17. Struchtrup, H.: Macroscopic Transport Equations for Rarefied Gas Flows. Springer, New York (2005)
18. Chapman, S., Cowling, T.G.: The Mathematical Theory of Nonuniform Gases. Cambridge University Press, (1970)
19. Grad, H.: On the kinetic theory of rarefied gases. Commun. Pure Appl.Math. **2**, 331 (1949)
20. Garcia, L., Velasco, R.M., Uribe, F.J.: Beyond the Navier–Stokes equations: Burnett hydrodynamics. Phys. Rep. **465**, 149 (2008)
21. Bobylev, A.V.: Instabilities in the Chapman-Enskog expansion and hyperbolic Burnett equations. J. Stat. Phys. **124**, 371 (2006)
22. Bobylev, A.V.: Generalized Burnett hydrodynamics. J. Stat. Phys. **132**, 569 (2008)
23. Bobylev, A.V., Windfall, A.: Boltzmann equation and hydrodynamics at the Burnett level. Kinet. Relat. Models **5**, 237 (2012)
24. Struchtrup, H., Torrilhon, M.: Regularization of Grad's 13 moment equations: derivation and linear analysis. Phys. Fluids **15**, 2668 (2003)
25. Struchtrup, H., Torrilhon, M.: Higher-order effects in rarefied channel flows. Phys. Rev. E **78**, 046301 (2008)
26. Struchtrup, H., Torrilhon, M.: Regularized 13 moment equations for hard sphere molecules: linear bulk equations. Phys. Fluids **25**, 052001 (2013)
27. Struchtrup, H., Torrilhon, M.: Boundary conditions for regularized 13-moment-equations for micro-channel-flows. J. Comput. Phys. **227**, 1982 (2008)
28. Rana, A.S., Torrilhon, M., Struchtrup, H.: A robust numerical method for the R13 equations of rarefied gas dynamics: application to lid driven cavity. J. Comput. Phys. **236**, 169 (2013)
29. Taheri, P., Torrilhon, M., Struchtrup, H.: Couette and Poiseuille microflows: analytical solutions for regularized 13-moment equations. Phys. Fluids **21**, 017102 (2009)
30. Cai, C.: Heat transfer in vacuum packaged microelectromechanical system devices. Phys. Fluids **20**, 017103 (2008)
31. Sone, Y.: Comment on "Heat transfer in vacuum packaged microelectromechanical system devices" [Phys. Fluids 20, 017103 (2008)], Phys. Fluids **21**, 119101 (2009)
32. Rana, A.S., Torrilhon, M., Struchtrup, H.: Heat transfer in micro devices packaged in partial vacuum. JPCS **362**, 012034 (2012)